

Exploring quasifission characteristics for $^{34}\text{S} + ^{232}\text{Th}$ forming ^{266}Sg

E. Prasad,^{*} A. Wakhle,[†] D. J. Hinde, E. Williams, M. Dasgupta, M. Evers,[‡] D. H. Luong, G. Mohanto,[§] C. Simenel, and K. Vo-Phuoc

Department of Nuclear Physics, Research School of Physics and Engineering, Australian National University, Canberra, ACT 2601, Australia

(Received 21 October 2015; published 12 February 2016)

Background: Fission fragments from heavy ion collisions with actinide nuclei show mass-asymmetric and mass-symmetric components. The relative probabilities of these two components vary rapidly with beam energy with respect to the capture barrier, indicating a strong dependence on the alignment of the deformed nucleus with the partner in the collisions.

Purpose: To study the characteristics of the mass-asymmetric quasifission component by reproducing the experimental mass-angle distributions to investigate mass evolution and sticking times.

Methods: Fission fragment mass-angle distributions were measured for the $^{34}\text{S} + ^{232}\text{Th}$ reaction. Simulations to match the measurements were made by using a classical phenomenological approach. Mass ratio distributions and angular distributions of the mass-asymmetric quasifission component were simultaneously fit to constrain the free parameters used in the simulation.

Results: The mass-asymmetric quasifission component—predominantly originating from tip (axial) collisions with the prolate deformed ^{232}Th —is found to be peaked near $A = 200$ at all energies and center-of-mass angles. A Monte Carlo model using the standard mass equilibration time constant of 5.2×10^{-21} s predicts more symmetric mass splits. Three different hypotheses assuming (i) a mass halt at $A = 200$, (ii) a slower mass equilibration time, or (iii) a Fermi-type mass drift function reproduced the main experimental features.

Conclusions: In tip collisions for the $^{34}\text{S} + ^{232}\text{Th}$ reaction, mass-asymmetric fission with $A \sim 200$ is the dominant outcome. The average sticking time is found to be $\sim 7 \times 10^{-21}$ s, independent of the scenario used for mass evolution.

DOI: [10.1103/PhysRevC.93.024607](https://doi.org/10.1103/PhysRevC.93.024607)

I. INTRODUCTION

Although the last stable element to be discovered was added to the periodic table nearly 100 years ago, the synthesis of new heavy elements and isotopes [1,2], and the study of their properties, continues to be a very important subject in nuclear physics. Impressive progress has been achieved, with superheavy elements ($Z \geq 104$) up to $Z = 118$ [1,2] having been created by using heavy ion fusion reactions.

Superheavy element (SHE) synthesis is very difficult due to very low production cross sections, often on the order of picobarns or less [1,2]. These low cross sections can partly be attributed to the presence of a nonequilibrium process called quasifission [3–5]. Quasifission is a fission-like process, where the intermediate system formed after capture reseparates before forming a compact, completely equilibrated compound nucleus (CN) [6]. Because reseparation occurs before CN formation, evaporation residue (ER) cross sections are reduced [7,8]. The selection of the optimum reaction for SHE synthesis

would be helped by a detailed understanding of the quasifission process. However, though considerable progress has been made, a quantitative model does not exist at the moment.

In 1981, Świątecki predicted that quasifission should occur in nuclear collisions with $Z_P Z_T \geq 1600$ [4], where Z_P and Z_T are the atomic numbers of the projectile and target nuclei, respectively. However, subsequent measurements using a variety of projectile-target combinations have reported the onset of quasifission in mass-asymmetric collisions with much lower $Z_P Z_T$ values [8]. Beyond the suppression of ER cross sections, quasifission signatures can also be observed in many other experimental fission observables, such as large fission-fragment mass widths [9–13], correlations between fission masses and observation angles [9,13–15], and large fission-fragment angular anisotropies incompatible with CN formation [13,16–18].

Quasifission is now understood to have a strong dependence on gross entrance channel properties such as mass asymmetry [8,19,20] and beam energy [21–24]. It has also been shown to be sensitive to nuclear structure effects—namely, static deformation [17,25–27], closed shells [28,29], and the N/Z matching of the projectile and target nuclei [28]. In addition, the fissility of the compound nucleus being formed has been found to play a role in quasifission outcomes [12,14]. However, the complex dependence of quasifission on these variables makes it difficult to understand this process completely. Despite its conceptual simplicity as a process intermediate between a deep-inelastic process and the formation of an equilibrated CN through true fusion, the measurement of quasifission is complicated by the fact that experimental quasifission observables overlap with those of fusion-fission.

^{*}Permanent address: Department of Physics, School of Mathematical and Physical Sciences, Central University of Kerala, Kasaragod 671314, India; prasad.edayillam@anu.edu.au

[†]Present Address: National Superconducting Cyclotron Laboratory, Michigan State University, Michigan 48824, USA.

[‡]Present Address: ANU College of Medicine, Biology and Environment, The John Curtin School of Medical Research, Canberra, ACT 2601, Australia.

[§]Present Address: Nuclear Physics Division, Bhabha Atomic Research Centre, Mumbai 400085, India.

Quantitative predictions of SHE cross sections for various reactions and bombarding energies require a detailed understanding of quasifission.

Quasifission is known to be an out-of-equilibrium dynamical process. As such, an important quantity that characterizes quasifission is its timescale—specifically, the time interval between projectile-target capture and the subsequent break up (scission). The other key timescale is that required for mass flow between the projectile-like and target-like nuclei, which results from the dependence of the potential on the mass-asymmetry. Crucially, these timescales were shown to be similar by Töke *et al.* in Ref. [3]. For this reason, experimental mass-angle distributions (MADs) of the fragments can provide direct evidence of the presence of quasifission in a reaction through the observation of a correlation [3,30] between the fragment mass and observation angle. Since this correlation is directly related to the characteristic timescales of the quasifission process, MADs can effectively be used [3,9,14,31] to obtain information on quasifission timescales.

In this work, we present a detailed study of mass-angle distributions for the reaction $^{34}\text{S} + ^{232}\text{Th}$ forming the compound system ^{266}Sg . This is part of a broader study of the role of the entrance channel fissility [14] (often termed mass asymmetry) in quasifission characteristics for reactions forming ^{266}Sg and ^{262}Rf , which will appear in a later presentation. The present measurement follows the study of fission-fragment mass-angle distributions and angular distributions for the $^{32}\text{S} + ^{232}\text{Th}$ reaction reported earlier [23]. MADs were measured for the $^{34}\text{S} + ^{232}\text{Th}$ reaction at energies around the capture barrier (7% below to 8% above) in finer beam-energy steps and were then compared with phenomenological calculations to obtain a quantitative understanding of the evolution of quasifission characteristics and timescales as a function of bombarding energy for this reaction.

The phenomenological model [14,31], using the same basis as Ref. [3], assumes classical trajectories for the incoming and outgoing nuclei and relates angular displacement to the sticking time through calculated angular-momentum distributions and moments of inertia. The analysis relies on two simple concepts: (i) the angular distribution of the fragments from the MAD provides information about the sticking-time distribution, and (ii) this time information combined with the measured mass distribution provides information on the mass evolution with time. The mass evolution function extracted in Ref. [3] was not able to reproduce the experimental results, thus different forms of mass evolution after capture have been investigated.

The paper is organized as follows: Experimental details, data analysis and experimental results are described in Secs. II, III, and IV, respectively. Details of the phenomenological model and the different underlying model assumptions proposed in this work are presented in Secs. V and VI, respectively, followed by a discussion on quasifission timescales in Sec. VII. We summarize our findings and conclude in Sec. VIII.

II. EXPERIMENTAL DETAILS

The experiment was performed at the Australian National University's Heavy Ion Accelerator Facility. Pulsed ^{34}S

beams with a pulse separation of 107 ns and a full width at half maximum (FWHM) of 0.7–1.5 ns from the 14UD Pelletron accelerator were used to bombard a ^{232}Th target of thickness $80 \mu\text{g}/\text{cm}^2$ with a $20 \mu\text{g}/\text{cm}^2$ carbon backing facing downstream. The target normal was oriented at 60° to the beam axis, which avoided shadowing the detectors and minimized the energy loss of the detected fission fragments. The measurements were performed at laboratory energies (after correcting for energy loss in the target) of 164.7, 167.2, 169.7, 172.7, 181.6, and 191.2 MeV.

Reaction products were detected using the Australian National University (ANU) CUBE spectrometer [25], which consists of two large-area position-sensitive multiwire proportional counters (MWPCs), each with an active area of $279 \times 357 \text{ mm}^2$. These MWPC detectors were mounted at 45° (front detector) and 90° (back detector) scattering angles with respect to the beam direction. The detectors were placed such that the normal to the central foil of each detector was at 180 mm from the target center, and at an azimuthal angle of 180° and 0° for the back and front detectors, respectively. Two silicon monitor detectors mounted at $\theta = 30^\circ$ (at azimuthal angles of 90° and 270°) were used to measure energies of the elastically scattered particles and for beam normalization.

III. DATA ANALYSIS

The MWPC detectors provided energy loss, position, and timing information. Position information for the particles reaching the detectors was obtained from the timing of signals from both ends of the detector X and Y wire planes using delay-line readouts. Fast timing information was obtained from the cathode foil of each detector and was measured with respect to the rf signal generating the beam pulses. The calibrated positions and the time-of-flight information were then used to obtain the fragment velocities and, assuming two-body kinematics [3,10,14,25], mass ratios and center-of-mass angles were extracted.

As the target nucleus used in this experiment has high fissility, three-body events such as transfer fission are expected to be significant, in addition to binary events such as scattering, deep inelastic and fission. While these binary events are characterized by the detection of full momentum transfer (FMT) during the reaction, transfer-fission events are not, since the presence of a third heavy nucleus destroys the binary-kinematic correlations. This difference is reflected in the velocity components of the fragments from the two different fission processes and is used to cleanly separate binary-fission events from transfer-fission and any other three-body events [23,25].

To identify the FMT events, the velocity components of the fragments parallel to the beam (v_{\parallel}) and in the plane perpendicular to the beam axis (v_{\perp}) were extracted event by event [23,25] and used to generate scatter plots [14,23] of $v_{\parallel} - v_{\text{cn}}$ versus v_{\perp} , where v_{cn} is the calculated CN velocity and is equal to the velocity of the center-of-mass frame. These scatter plots are shown in Figs 1(a) to 1(f), where the mass ratios close to the entrance channel have been excluded.

FMT (two-body) events are peaked at $v_{\parallel} = v_{\text{cn}}$ and $v_{\perp} = 0$. Values of $v_{\parallel} - v_{\text{cn}}$ and v_{\perp} for transfer-fission events in general

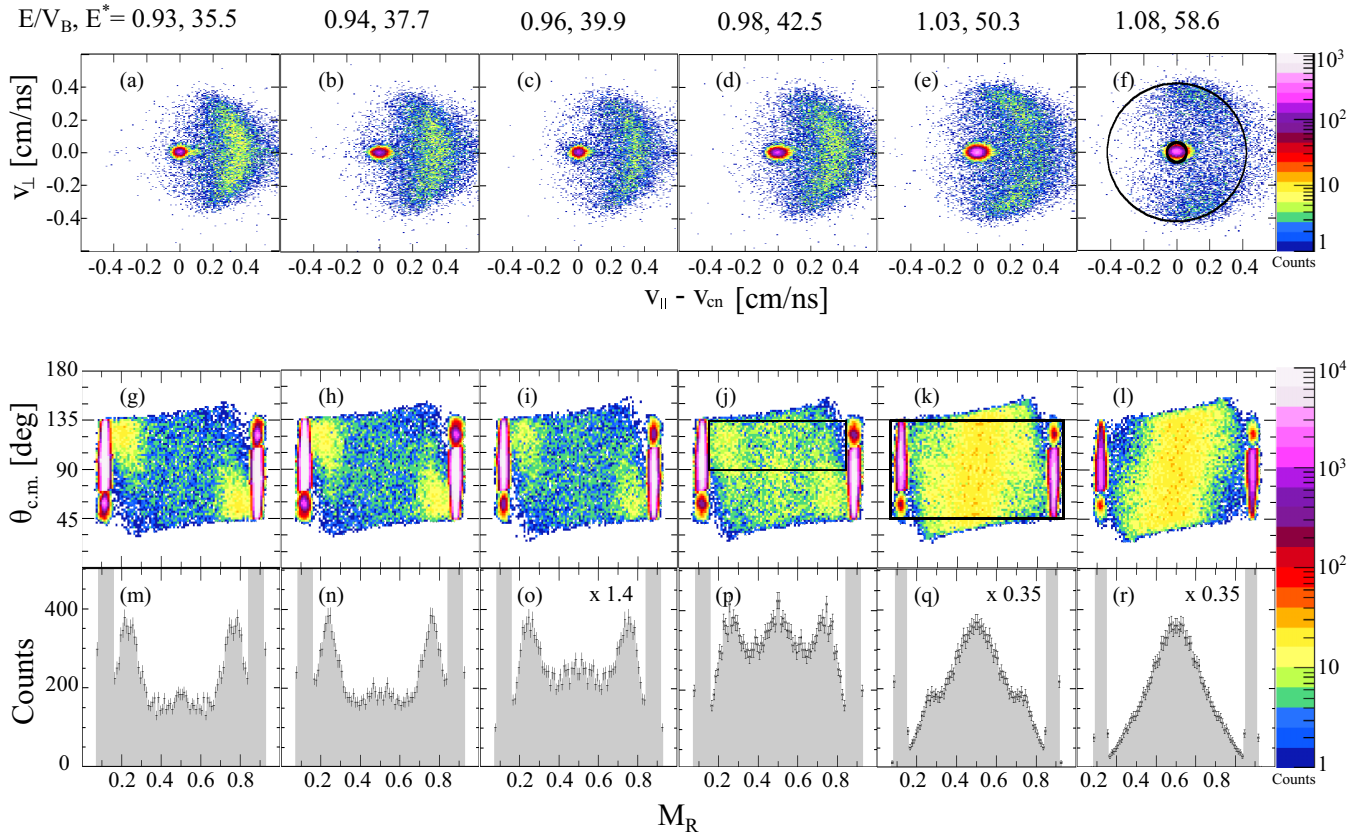


FIG. 1. Upper panels (a) to (f) show $v_{\parallel}-v_{\text{cn}}$ versus v_{\perp} scatter plot for all fission events, at different beam energies. The E/V_B values ($V_B = 154.8$ MeV) and CN excitation energies E^* are given at the top of each plot. Central panels (g) to (l) show experimental MAD scatter plots for $^{34}\text{S} + ^{232}\text{Th}$ reactions at different energies. Lower panels (m) to (r) show the corresponding projected M_R distributions of the mirrored MADs shown in panels (g) to (l). The angular window ($45^\circ < \theta_{\text{c.m.}} < 135^\circ$) used for producing these M_R distributions is indicated in panel (k).

are constrained by kinematical limits that depend on the momentum of the recoiling projectile-like nucleus. Thus, transfer-fission events are generally expected to be scattered inside a circle of radius v_{cn} [shown as outer circle in Fig. 1(f), for example], with its center at $v_{\parallel} = v_{\text{cn}}$ and $v_{\perp} = 0$. The only circumstance allowing transfer fission events to occupy the position of FMT fission events is where the projectile-like nucleus recoils at a center-of-mass angle such that $v_{\parallel} = v_{\text{cn}}$, and the subsequent fission of the target-like nucleus occurs in the plane of the transfer reaction, giving $v_{\perp} = 0$. By applying a tight gate on the FMT events, the background of transfer-fission events is estimated to be less than 1% at all beam energies.

Energy loss corrections for the beam particles as well as for the fission fragments produced in the reaction were included, assuming that interactions occurred at the center of the target. The fragment mass ratio M_R for a fission fragment observed in the back-angle detector was then obtained by using the following expression:

$$M_R = \frac{m_1}{m_1 + m_2} = \frac{v_2}{v_1 + v_2}, \quad (1)$$

where m_1 and m_2 are the fragment masses at scission and v_1 and v_2 are the velocities in the center-of-mass frame for the fragments detected in the back and front detectors, respectively [14]. Particle evaporation from the fragments does

not alter the centroids of the mass ratio distribution, because the mass ratio is derived from the fragment velocities, which—on average—are not affected by the evaporation of light particles. The corresponding center-of-mass angle $\theta_{\text{c.m.}}$ could then be determined.

MADs of fission-like fragments were evaluated at all measured energies; further details regarding the extraction of MAD can be found in Ref. [14]. Since we detected both fragments for each event, the mass-angle matrix was populated at $(M_R, \theta_{\text{c.m.}})$ and $(1 - M_R, \pi - \theta_{\text{c.m.}})$; the latter corresponding to the fission fragment incident on the forward-angle MWPC.

IV. EXPERIMENTAL RESULTS

MADs extracted for the $^{34}\text{S} + ^{232}\text{Th}$ reaction at each beam energy are shown in Figs. 1(g) to 1(l). The CN excitation energies and E/V_B values are given in the top panels (a) to (f), where E is the center-of-mass energy and V_B is the capture barrier ($V_B = 154.8$ MeV in this case) from calculations [32] optimized for heavy systems. The total M_R distributions were obtained by projecting these experimental MADs onto the M_R axis, shown in the lower panels (m) to (r) of Fig. 1. An angular window ($\theta_{\text{c.m.}}$) of 90° has been used [$45^\circ \leq \theta_{\text{c.m.}} \leq 135^\circ$, as shown in Fig. 1(k)] when projecting the MADs to avoid

biasing the data due to the geometrical limits of the detectors' angular acceptance.

Experimental MADs presented in Fig. 1 consist of different groups originating from quasi-elastic, deep-inelastic, quasi-fission, and fusion-fission processes. The events appearing at the M_R values corresponding to those expected from the entrance channel projectile and target masses originate from elastic, quasi-elastic, and deep-inelastic events. The latter are characterized by strong energy dissipation but weak mass drift away from the entrance channel mass asymmetry [33,34]. Because the focus of this article is on fission, other classes of binary event without significant mass flow are not discussed further.

The changing features of the MADs presented in Figs. 1(g) to 1(l) clearly demonstrate the systematic variation of binary fragmentation outcome with beam energy in the $^{34}\text{S} + ^{232}\text{Th}$ reaction. The strong mass-asymmetric components, clearly visible in Figs. 1(g) and 1(h) as yellow areas, represent fast reseparation after capture, indicating memory of the entrance channels masses and angles. The change of mass evolution with beam energy can be seen by comparing Figs. 1(g) and 1(h) to Figs. 1(k) and 1(l), where a peaked mass-symmetric component becomes significant. The relative variation of mass-asymmetric and mass-symmetric components with beam energy is clearly seen from their respective M_R projections in Figs. 1(m) to 1(r).

This changing pattern of the MAD and mass distributions with beam energy has been reported earlier for the $^{32}\text{S} + ^{232}\text{Th}$ [23] and $^{36}\text{S} + ^{238}\text{U}$ [21] reactions. The beam energy dependence from below the capture barrier to above has been explained qualitatively in terms of the deformation alignment [25,26] of the prolate target nuclei used in these reactions. At energies below the capture barrier, collisions with the tip of the deformed target nucleus (axial collisions) are dominant. Because the elongation is far outside the saddle point in such cases, the system typically reseparates soon after capture without full mass equilibration, leading to mass-asymmetric quasifission. On the other hand, in the case of equatorial collisions, which contribute significantly only at energies above the barrier, the contact configuration is more compact. This more compact configuration is presumably the reason that the system sticks together for a longer time, resulting in more complete mass equilibration [23,25]. More recently, TDHF calculations for the $^{40}\text{Ca} + ^{238}\text{U}$ reaction [15] have provided confirmation from a microscopic basis for this picture.

In this paper, we seek to quantify the mass-asymmetric quasifission component observed in the experimental MADs and estimate the timescales associated with these quasifission events by reproducing the experimental features in a phenomenological classical simulation.

The first step in this procedure is to make an empirical analysis of the mass ratio spectra. This starts with the unmirrored mass ratio spectra, corresponding to the angular range $90^\circ \leq \theta_{\text{c.m.}} \leq 135^\circ$. The M_R distribution at $E/V_B = 0.98$ (excluding the quasi-elastic component) is shown in Fig. 2 as an example. To extract the empirical trends of the data, these distributions were fit with three Gaussian functions (red dashed line for the mass-symmetric component and green dot-dashed line for mass-asymmetric components), as shown in Fig. 2.

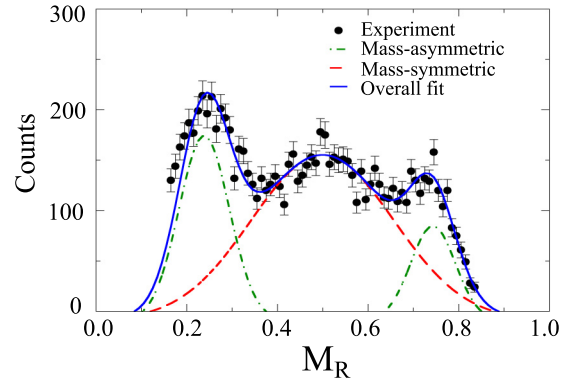


FIG. 2. Unsymmetrized M_R distribution of the fragments from $^{34}\text{S} + ^{232}\text{Th}$ at $E^* = 42.5$ MeV, for $90^\circ \leq \theta_{\text{c.m.}} \leq 135^\circ$. The red dashed and green dot-dashed lines correspond to individual Gaussian fits while the solid blue line represents the overall fit.

The solid blue line represents the overall fit. The central broad peak is centered close to $M_R = 0.5$ and represents fusion-fission and mass-symmetric quasifission events [23]. The peaks on either side comprise the mass-asymmetric fast quasifission components. The centroids of the Gaussians give a representation of the average mass of each component, and the area of each Gaussian represents the number of events that fall into the measured angular range. It must be noted that the number of events cannot be translated directly to cross sections since the fast quasifission angular distribution can vary significantly with beam energy and be sharply peaked in angle, as will be discussed later. This is in contrast with fusion-fission, where the angular distribution can be estimated by using the transition-state model [35]. Thus, a narrow experimental angular acceptance can lead to significant uncertainties in estimating the total fast quasifission yield. Even the 90° acceptance in $\theta_{\text{c.m.}}$ of the present experiment would require extrapolation to angles closer to the beam axis to obtain the most reliable relative probabilities for the mass-asymmetric and mass-symmetric components.

The average M_R values of the heavy mass-asymmetric peak and the symmetric peak as a function of E/V_B are shown in Fig. 3. The mass-symmetric component has average M_R values scattered around 0.5, corresponding to a pre-evaporation mass of $A = 133$. The heavy asymmetric component has an average pre-evaporation mass between 200 and 208, which shows a weak dependence on energy with respect to the capture barrier. The upward arrows shown in this figure indicate the energies selected for the comparison with the phenomenological simulations, discussed in Sec. V.

Although the relative intensities of each peak vary with energy, the centroids are almost independent of beam energy. This allows summing of MADs from the three lowest energies to increase statistics, to permit the extraction of the angle dependence of the components. Angular bins of width 5° in $\theta_{\text{c.m.}}$ were applied to the sum of the MADs at the three lowest energies, and the resulting mass ratio spectra were fit as above. The M_R values of the centroids of the Gaussian peaks are shown as a function of center-of-mass angle in Fig. 4 for the mass-symmetric and heavy mass-asymmetric components.

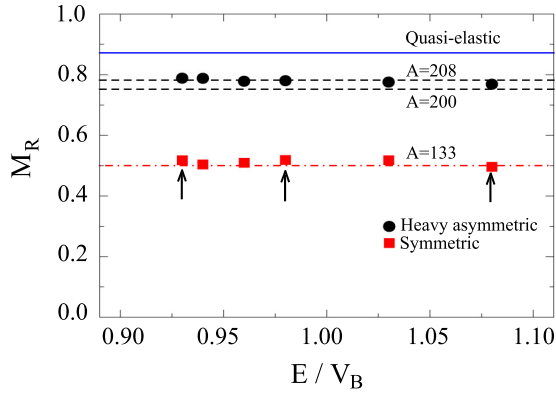


FIG. 3. Average mass ratio of the heavy asymmetric fragments and symmetric fragments measured as a function of E/V_B . Dot-dashed (red) line represents pre-evaporation mass $A = 133$ (symmetric fission) and upper and lower broken lines (black) represent $A = 208$ and 200 , respectively and the solid (blue) line represents the entrance channel mass asymmetry. Upward arrows represent three data points selected for the theoretical simulations discussed in Sec. V.

The vertical bars correspond to the widths (σ_{MR}) of the respective Gaussian distributions. The dependence on center-of-mass angle of the centroid of the mass-asymmetric component is very weak, and is a key feature of the data. As discussed below, this suggests an avenue for a phenomenological approach to extract the timescales for this component.

Figure 4 shows that, at all angles, the mass-asymmetric peak is distinct from the mass-symmetric component. Thus, by gating on the mass-asymmetric region in the MAD for either the light or the heavy fragment, the angular distribution of this component can be extracted, which will be sensitive to the sticking-time distribution. This approach, and the results obtained, are described in the next section.

V. MONTE CARLO SIMULATION OF THE MAD

In order to determine the characteristic timescales of the observed mass-asymmetric quasifission, we followed a

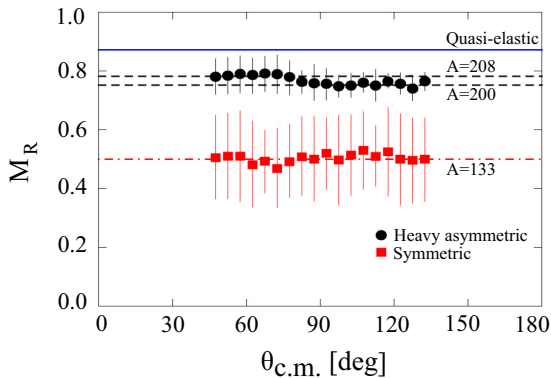


FIG. 4. The dependence on the center-of-mass angle ($\theta_{c.m.}$) of the average mass ratio for the heavy asymmetric and symmetric fragments for the $^{34}\text{S} + ^{232}\text{Th}$ reaction at the three lowest measured energies. Vertical bars indicate the widths (σ_{MR}) of the Gaussian fits.

classical phenomenological approach [3,14] to simulate the major features of the experimental MADs. Within this model, we first try the standard prescription [3] for mass evolution as a function of time and show that it completely fails to reproduce the experimental results observed in this study. We then propose three different hypotheses to reproduce the experimental MADs, M_R distributions, and the angular distributions of the mass-asymmetric quasifission component. The details of the model, the major observations, and the conclusions are discussed in the following sections.

A. Basis of simulation

The population of a given bin in the mass-angle distribution depends on (i) the distribution of angles between the beam axis and the line joining the centers of the projectile and target nuclei at contact, (ii) the distribution of rotation angles, and (iii) the mass evolution after contact [3,9,14,31]. To calculate the angle at which a given event will be observed, it is assumed that the colliding nuclei follow Coulomb trajectories until contact. The combined system rotates through an angle $\Theta_{\text{rot}}(t_s)$ after capture, reseparating after a period t_s (the sticking time). The separate fragments then move along Coulomb trajectories to infinity, defining the final scattering angle in the center-of-mass frame.

The final scattering angle of the projectile-like nucleus $\theta_{\text{sc}}(t_s)$ is related to the rotation angle $\Theta_{\text{rot}}(t_s)$ through the relation [9,14]

$$\theta_{\text{sc}}(t_s) = \pi - \Theta_{\text{in}} - \Theta_{\text{out}} - \Theta_{\text{rot}}(t_s), \quad (2)$$

where Θ_{in} and Θ_{out} are the angles associated with the Coulomb trajectories for the incoming and outgoing nuclei, calculated from the impact parameter and distance of closest approach [14], and taking into account the change in masses while the system is rotating.

The angle of rotation $\Theta_{\text{rot}} = \omega \times t_s$, where ω is the angular velocity, which is related to the angular momentum L and the mean moment of inertia I through

$$\omega = \frac{L}{I}. \quad (3)$$

Capture angular-momentum distributions [36] were calculated in the coupled channels framework, and quasifission moments of inertia were calculated by using the time-dependent Hartree-Fock (TDHF) framework [37,38] allowing a quantitative approach to calculating distributions of ω , and thus Θ_{rot} and θ_{sc} .

It is well accepted that the mass-asymmetric quasifission that we observe, which is most prevalent at energies below the average capture barrier, is associated with axial (tip) collisions with a prolate deformed target nucleus. Accordingly, the MAD simulations were carried out separately for the axial and equatorial collisions in this work, using appropriate angular-momentum distributions as described below. The MAD histograms thus generated were combined to produce the final MADs.

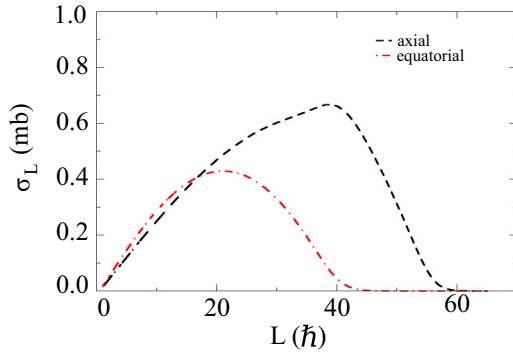


FIG. 5. Typical angular momentum-distributions generated for the axial and equatorial collisions for the $^{34}\text{S} + ^{232}\text{Th}$ reaction at $E/V_B = 0.98$, where L and σ_L are the angular momentum and partial-wave cross sections, respectively.

B. Angular momentum

The capture angular-momentum distributions were calculated by using the coupled channels code CCMOD [39], a version of CCFUS [40]. The nuclear potential was adjusted to reproduce the experimental average capture barrier for the $^{32}\text{S} + ^{232}\text{Th}$ reaction [23].

As in Ref. [25], collisions up to a critical angle (θ_{crit}) between the projectile direction and the target deformation axis were taken as tip collisions, which in the present reaction $^{32}\text{S} + ^{232}\text{Th}$ were assumed to result in fast quasifission. We took $\theta_{\text{crit}} = 25^\circ$ in this work, guided by the relative yields of fast and slow fission at near-barrier energies. The analysis of relative yields will be described in a separate presentation, currently in preparation.

For each beam energy, separate capture angular-momentum distributions were generated for collisions up to θ_{crit} (tip collisions) and from θ_{crit} to 90° (side collisions). Typical angular-momentum distributions generated using the coupled channels calculation for the axial and equatorial collisions at $E/V_B = 0.98$ are shown in Fig. 5. These angular-momentum distributions were used for generating the fast and slow quasifission MADs, respectively.

C. Moment of inertia

We used an average rigid body moment of inertia (I) during the sticking phase, obtained from TDHF calculations. Time-dependent I values were calculated by finding the rigid body moment of inertia at each time step by using TDHF densities [37,38]. Calculations were performed with a time step of 1.5×10^{-24} s. The SLy4d [41] parametrization of the Skyrme interaction was used in these calculations. Calculated I values normalized by the moment of inertia of a rigid sphere I_0 ($I_0 = \frac{2}{5}AR_0^2$ where A is the total mass of the nonspherical system and $R_0 = 1.225 A^{1/3}$ [42]) are shown in Fig. 6, for representative beam energies (center-of-mass), angular momenta, and orientations. The average moment of inertia between 2 zs and 13 zs, where 1 zs = 10^{-21} s, was used in the fast quasifission simulations.

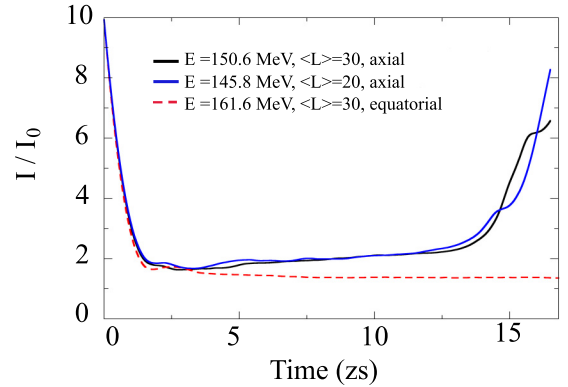


FIG. 6. TDHF calculations of moments of inertia, normalized by the moment of inertia of a rigid sphere, I_0 , as a function of time in zeptoseconds, for different beam energies (center-of-mass). The orientation (axial or equatorial) and average angular-momentum value used in each case are indicated. The average value of I/I_0 between 2 zs and 13 zs was used in the quasifission simulations.

D. Mass drift

To describe the mass drift towards mass symmetry with time, we initially used the exponential function proposed in Ref. [3], which describes an asymptotic approach to mass symmetry ($M_R = 0.5$) with an initial rapid rate of change. The average value of M_R after a sticking time t_s is given by

$$M_R(t) = [M_R(0) - 0.5]e^{-t_s/\tau_m} + 0.5, \quad (4)$$

where $M_R(0)$ is the initial mass ratio before mass flow starts, given by $M_R(0) = A_T/(A_T + A_P)$ (here A_T and A_P are the target and projectile masses, respectively). The mass equilibration time constant was initially taken to have the value $\tau_m = 5.2$ zs, consistent with Ref. [3]. A time delay τ_d before mass equilibration starts can be included by subtracting τ_d from τ_s , and fixing $M_R = M_R(0)$ until after τ_d . The standard [3] curve for mass-evolution as a function of time [following Eq. (4)] is shown in Fig. 7(b), with an initial delay of 1 zs. Variations in the parameters and form of the expression for $M_R(t)$ have been tested in this work, which will be discussed below.

Fluctuations in the values of $M_R(t)$ have been applied to provide a more realistic comparison to the data, as described in Ref. [14]. The fluctuations are generated by using a random Gaussian form of deviation from the smooth expression for $M_R(t)$, with the sigma varying linearly from $\sigma_{MR} = 0.025$ at the initial mass split to $\sigma_{MR} = 0.1$ at mass symmetry [14]. The good reproduction of experiment with this parametrization meant that the effect of changing this assumed behavior was not explored.

E. Sticking-time distributions

For each simulated event, the M_R values were calculated by using a randomly chosen sticking time t_s , following a distribution assumed to be a half-Gaussian function followed by an exponential fall, characterized by the Gaussian peak position (p), sigma (s) and an exponential fall time (e). The parameters p , s , and e were varied to reproduce the features of

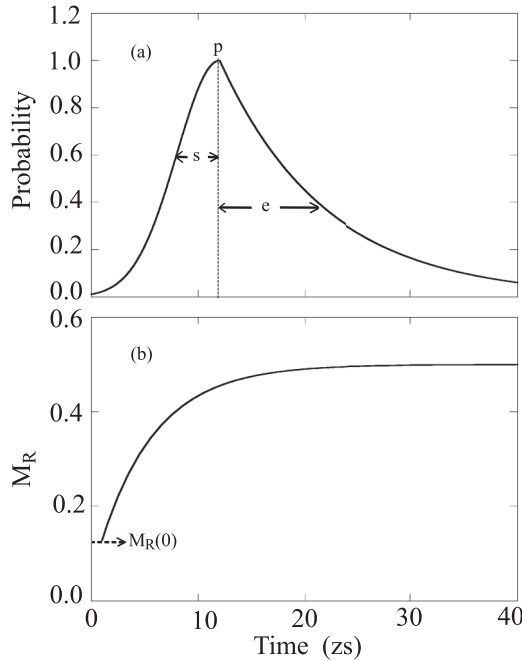


FIG. 7. (a) Typical sticking-time distribution with parameters $(p, s, e) = (12, 4, 10)$ zs as indicated (see text; Sec. V E). (b) M_R evolution as a function of time following Eq. (4), with an initial time delay of 1 zs.

the experimental MAD. A typical t_s distribution with $p = 12$ zs, $s = 4$ zs, and $e = 10$ zs is shown in Fig. 7(a).

As axial collisions result primarily in faster reseparation in comparison to equatorial collisions, different time distributions as well as different angular-momentum distributions were used for the two quasifission components. A faster t_s distribution was selected for the axial collisions and a relatively slower distribution was used for the equatorial collisions. Axial collisions are hereafter described as fast collisions and equatorial collisions as slow collisions.

The Gaussian fit parameters of the mass-symmetric component at the lowest energies indicated no significant correlation of mass with angle. This implies that such events typically complete one or more full rotations before scission. Hence a long t_s distribution should be chosen to allow the system enough time to complete one or more rotations before reseparation. With this in mind, a t_s distribution with $(p, s, e) = (24, 8, 20)$ zs, has been used for the slow events for all simulations. The detailed choice of the parameters is arbitrary because there is no significant correlation of mass with angle for such long sticking-time distributions. The parameter selection for the fast (tip) collisions requires more reaction-specific tuning, constrained by reproducing the experimental mass ratio distributions and angular distributions of the fast quasifission component, as discussed below.

F. Simulations with standard parameters

First, we attempted to reproduce the experimental MADs by using the mass evolution described in Eq. (4) with standard parameters to describe the fast quasifission resulting from

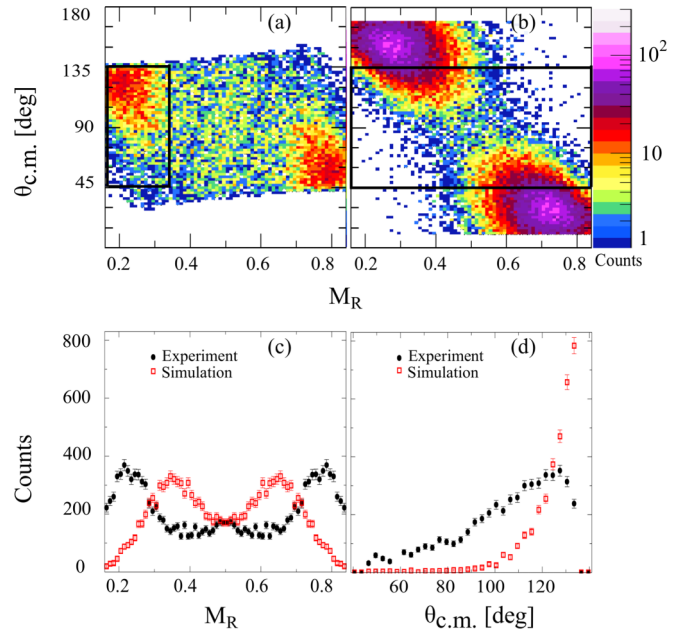


FIG. 8. (a) Experimental MAD at $E/V_B = 0.93$ (excluding the quasi-elastics). (b) MAD simulated (excluding quasi-elastics) for the same E/V_B assuming the exponential mass drift as given in Eq. (4). (c) M_R distributions of the experimental (filled black circles) and simulated (open red squares) MADs between the angular window 45° and 135° . The angular window used is shown as a rectangle in Fig. 8(b). (d) Angular distributions of the mass-asymmetric quasifission component present in this reaction. The angular and M_R window used are shown as rectangles in Fig. 8(a).

tip collisions. It was found that, to reach the observed angles, the sticking times were long enough that the fission mass ratio approached symmetry. The experimental MAD for the subbarrier measurement at $E/V_B = 0.93$ is shown in Fig. 8(a). Quasi-elastic events ($M_R < 0.16$ and $M_R > 0.84$) are excluded in this figure, and in those presented hereafter. The MAD simulation giving the best compromise between reproducing the mass and angle correlation in the data is shown in Fig. 8(b).

In comparing Figs. 8(a) and 8(b), it is clear that the simulation provides a poor description of the experiment. To quantify the disagreement, the M_R distributions of the experimental and simulated MADs are compared in Fig. 8(c). The rectangular window (45° to 135°) used to generate the M_R distributions is shown in Fig. 8(b). Similarly, the angular distributions in the region of the mass-asymmetric peak seen experimentally are compared in Fig. 8(d). An M_R window between 0.16 and 0.36 was applied as shown in Fig. 8(a).

The basic features of this experimental MAD cannot be reproduced by using the mass evolution described in Eq. (4), irrespective of the t_s distribution used. Figure 8(b) shows clearly that, by using the mass-equilibration time constant of 5.2 zs of Ref. [3], the calculated mass evolution towards symmetry is too rapid to produce events at angles and mass ratios observed in the experiment. Below, a number of alternative approaches are described that better reproduce the

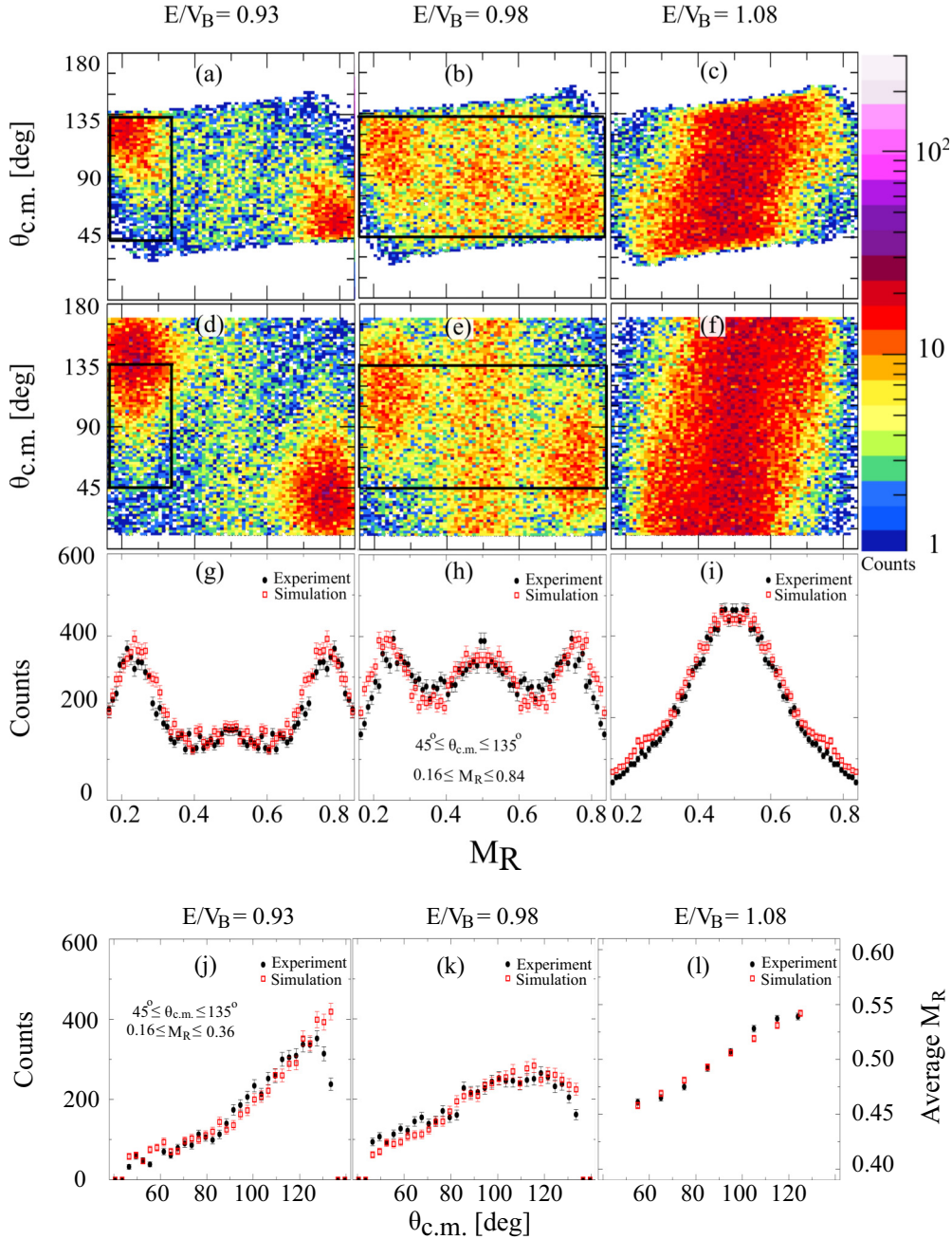


FIG. 9. Top Panels (a) to (c) show experimental MAD scatter plots for the $^{34}\text{S} + ^{232}\text{Th}$ reaction at different E/V_B , showing M_R values between 0.16 and 0.84. Panels (d) to (f) show simulated MADs at the same E/V_B values and M_R range, assuming mass evolution only to $A = 200$. Panels (g) to (i) show projected M_R distributions of experimental (filled black circles) and simulated (open red squares) MADs within the angular window 45° and 135° . The angular window used is shown as a rectangle in panels (b) and (e). Bottom panels (j) and (k) show angular distributions of mass-asymmetric quasifission events from experimental (filled black circles) and simulated (open red squares) MADs at $E/V_B = 0.93$ and 0.98 . The events are selected between the angular window 45° and 135° and M_R window 0.16 and 0.36, represented as rectangles in Figs. 9(a) and 9(d). Bottom panel (l) shows mean M_R as a function of center-of-mass angle at $E/V_B = 1.08$.

experimental MADs over the range of energies measured in this work.

VI. ALTERNATIVE APPROACHES TO MASS EVOLUTION

Three different approaches employed to reproduce the experimental MADs are discussed in this section. To get a clear picture of the variation of mass drift and angular distributions

with beam energy, simulations have been performed for the three energies, $E/V_B = 0.93, 0.98$ and 1.08 , as indicated by the arrows in Fig. 3. These span the average fusion barrier energy and give quite different features in the experimental MADs.

Although different sets of parameters can reproduce either the mass or angle spectra presented with the MADs in Fig. 9, the parameter space is drastically reduced by requiring the

simultaneous reproduction of both the M_R distributions and the angular distributions of the mass-asymmetric quasifission component. In the three different approaches described below, mass evolution of the slow quasifission events resulting from equatorial collisions is simulated as described above. The data are not sensitive to the time distribution chosen, as long as it allows almost complete mass drift to symmetry.

A. Mass evolution only to $A = 200$

One option to slow down the mass evolution is to halt mass evolution at the position of the experimentally observed peak in M_R . Therefore, all fast quasifission events are taken to evolve towards an M_R value corresponding to $A \sim 200$. A qualitative conjecture to explain this behavior is the following: fast events, during their evolution from $M_R(0)$ to mass-symmetry through a parabolic potential, may encounter a potential pocket around the M_R value corresponding to $A \sim 200$, originating from the large shell-correction energies in the ^{208}Pb region. This could provide an energetically favorable pathway to scission.

The simulations for the three selected E/V_B values are shown in Figs. 9(d) to 9(f). They can be compared with the experimental MADs shown immediately above them in Figs. 9(a) to 9(c). Only the M_R range between 0.16 and 0.84 is shown, to eliminate elastic and quasi-elastic events from the experimental MADs. The projections of the experimental and simulated MADs at each energy are shown in Figs. 9(g) to 9(i). The angular window used to generate the M_R distributions are shown as rectangles in Figs. 9(b) and 9(e), while the mass-angle gate used to generate the angle spectra for the mass-asymmetric component [shown in Figs. 9(j) and 9(k)] is shown in Figs. 9(a) and 9(d).

The contribution from mass-asymmetric quasifission is relatively small at the highest energy, which restricted use of the angular distribution of these events to extract meaningful timing information at this energy. Hence, a different method was employed to compare the MADs at this energy. The MAD was sliced into angular bins, each of width 10° in the center-of-mass frame, and the mean M_R of each bin was evaluated. The average M_R value is plotted against the mean center-of-mass angle as shown in Fig. 9(l). The slope of this distribution provides a measure of the characteristic correlation of mean mass with angle seen in the MAD.

The adopted mass evolution function is shown in Fig. 10(a), approaching the asymptotic value corresponding to $A = 200$ with the standard characteristic time of 5.2 zs. The adopted sticking-time distributions for the three increasing beam energies are shown (red dotted line) in Figs. 10(b), 10(c), and 10(d). With these adopted mass evolution and sticking-time functions, the features of the experimental and simulated MADs match quite well, as do the mass and angular distributions. The detailed shapes of the functions are unlikely to be uniquely specified by the adopted procedure but, as will be seen from the functions found for different mass-equilibration assumptions, the mean sticking times are well defined, with the main uncertainty likely to lie in the calculated capture angular-momentum distributions and possibly the moments of inertia.

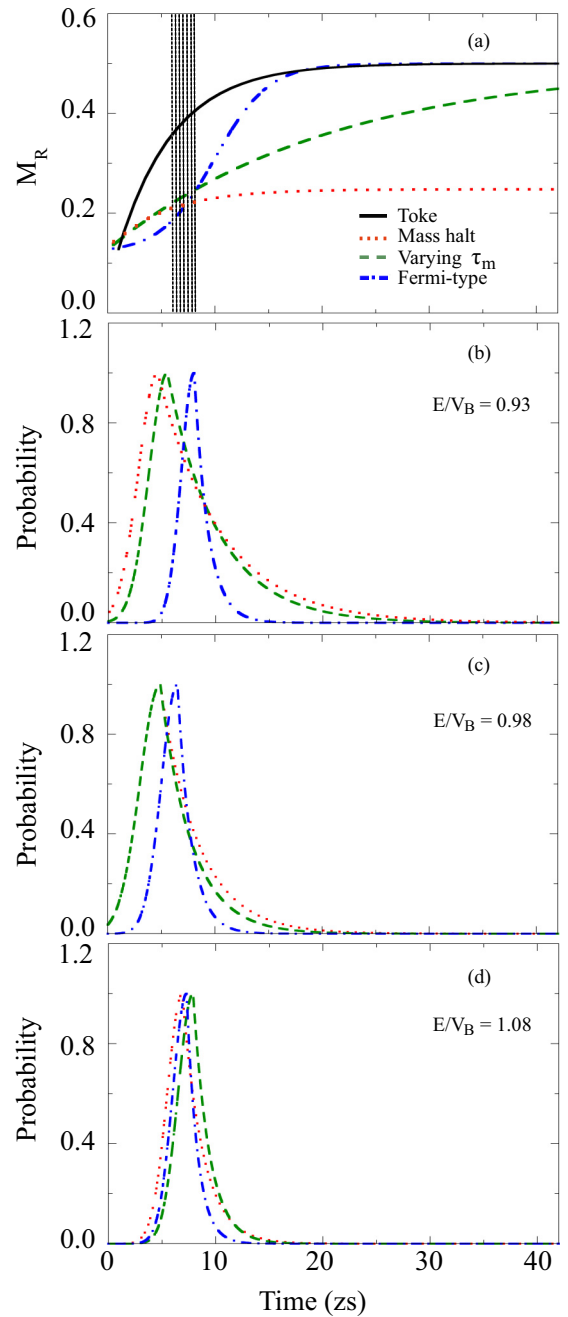


FIG. 10. (a) Mass drift as a function of time in Töke's picture [3], and three new scenarios presented in this work. The shaded region represents the average sticking time observed in this work (see Table I). Panels (b)–(d) show the sticking-time distributions of fast events at different E/V_B values as a function of time.

A question is why the equatorial collisions seem to be unaffected by the assumed shell effect at $A \sim 200$. Independent of the initial conditions of the collision, the system evolves in shape over the same potential-energy surface. However, since the axial and equatorial collisions show very different outcomes, they must follow different paths in deformation space. It is possible that the equatorial collisions do not encounter the potential valley near $A = 200$. The TDHF

calculations of Ref. [15] for the $^{40}\text{Ca} + ^{238}\text{U}$ reaction show such a bifurcation in outcomes, with the equatorial collisions undergoing much more mass equilibration than the axial collisions, as is seen experimentally.

The mass halt scenario of mass evolution for fast quasifission clearly can reproduce the main features of the experimental MADs. However, we now present two other approaches that also provide reasonable representations of the experimental MADs.

B. Varying τ_m for fast quasifission

Here we take the mass-equilibration time constant τ_m in Eq. (4) as a variable to be adjusted to obtain the optimum reproduction of experiment. The mass is assumed to evolve to symmetry. It was found that an energy-dependent τ_m value for fast quasifission gives the best reproduction of the M_R and angular distributions, varying from 21 zs at the lowest energy, through 12 zs to 10 zs at the highest energy. This may simply be a reflection of the fact that a feature in the potential-energy surface due to the increased binding around ^{208}Pb does play a role, and this effect is not included in this picture.

Figure 11 shows the simulated MADs at the three different E/V_B values, with the corresponding M_R distributions, angular distributions of mass-asymmetric quasifission events at $E/V_B = 0.93$ and 0.98 MeV, and the slope of the MAD at $E/V_B = 1.08$. Reasonable agreement between the experimental data and simulated results can be seen at all E/V_B values. The adopted mass evolution and sticking-time functions are shown (green dashed lines) in Fig. 10.

C. Mass evolution following a Fermi function

In the mass evolution functions used above, the exponential function originally proposed by Töke *et al.* [3] was applied. In that work, and subsequently, it was suggested [3,9] there should be a time delay of ~ 1 to 2 zs before and after the mass drift. These delays were interpreted as the time from contact to a sizable neck formation in the beginning and the time of neck constriction before scission. Recent TDHF calculations also reported an initial delay of ≤ 2 zs required for N/Z equilibration [28] in the $^{40}\text{Ca} + ^{208}\text{Pb}$ reaction before a significant mass drift. Similar observations were also reported in multinucleon transfer processes in the same reaction [43].

In order to model a slow mass drift during neck formation and neck constriction, we replaced the exponential mass-evolution function by a Fermi-type function, as shown (blue dot-dashed line) in Fig. 10(a). The form of this function was mainly decided by two parameters: a parameter related to its slope and another related to the time at which mass transfer reaches 50% of maximum. A third parameter was used to ensure the saturation at mass symmetry after a sufficiently long time. In order to reduce the number of free parameters used in the simulation, these three parameters were made interdependent. This is done by defining the parameters for slope and saturation in terms of the time at which mass transfer is 50%, using fixed scaling factors.

To reproduce the experimental features observed in the experimental MADs, the t_s distribution was varied for the fast events. The mean of the Fermi function was also adjusted to fit the experimental mass spectrum. Although a constant mean (8 zs) is found to reproduce the data at $E/V_B = 0.98$ and 1.08 , a slightly higher value (10 zs) was required for the data at $E/V_B = 0.93$. Figure 12 shows the simulated MADs at three different E/V_B values, corresponding M_R distributions, angular distributions of mass-asymmetric quasifission events at $E/V_B = 0.93$ and 0.98 , and the slope of the MAD at $E/V_B = 1.08$. Reasonable agreement between the experimental data and simulated results may be seen at all E/V_B values. The adopted mass evolution and sticking-time functions are shown (blue dot-dashed lines) in Fig. 10. Because the functional form of the mass evolution is different from the previous approaches [as seen in Fig. 10(a)], a peaked mass distribution for the fast quasifission events requires a much narrower sticking-time distribution. This is noticeable in Figs. 10(b) and 10(c).

VII. TIMESCALES OF FAST QUASIFISSION

The sticking-time distributions used to reproduce the MADs provide a representative measure of the reaction times associated with the fast and slow reaction components in $^{34}\text{S} + ^{232}\text{Th}$ reaction. Despite the conceptual differences imposed on the fast events through different mass-evolution scenarios presented in this work, all three consistently reproduced the experimental results with similar sticking-time distributions. This arises because once the experimental mass ratio distributions are well reproduced, the sticking-time distributions are determined predominantly by the angular distributions.

One important conclusion of this work centers on the sticking time t_s of fast quasifission events. These events are expected to result from separation relatively soon after contact, without achieving significant mass equilibration. The sticking-time distributions of these fast events at different E/V_B values are shown in Figs. 10(b)–10(d), which show differences in shape, but similar average values.

These average values of the t_s distribution, for the three pictures discussed in this work, at the three selected E/V_B values, are given in Table I. It may be noted that at the same E/V_B value, all three pictures have similar average t_s values. The t_s distributions have a relatively longer exponential tail at $E/V_B = 0.93$ and 0.98 , in the pictures assuming mass halt at $A = 200$ and energy-dependent τ_m values. However, the gross features of the MAD are weakly sensitive to slight variations of this exponential tail. The longer exponential tail is absent in the picture using a Fermi-type function for the mass drift. At the highest energy ($E/V_B = 1.08$), all three formalisms gave similar fast t_s distributions with the average values lying between 7–8 zs.

Given the simplicity of the phenomenological model used here, it is interesting to compare present results with those obtained with a fully dynamical model, TDHF. In the TDHF calculations reported in this work the sticking times were 10–12 zs. While this timescale range is $\sim 60\%$ longer than that obtained with the simple model, the agreement is surprisingly good given the simplicity of our phenomenological approach.

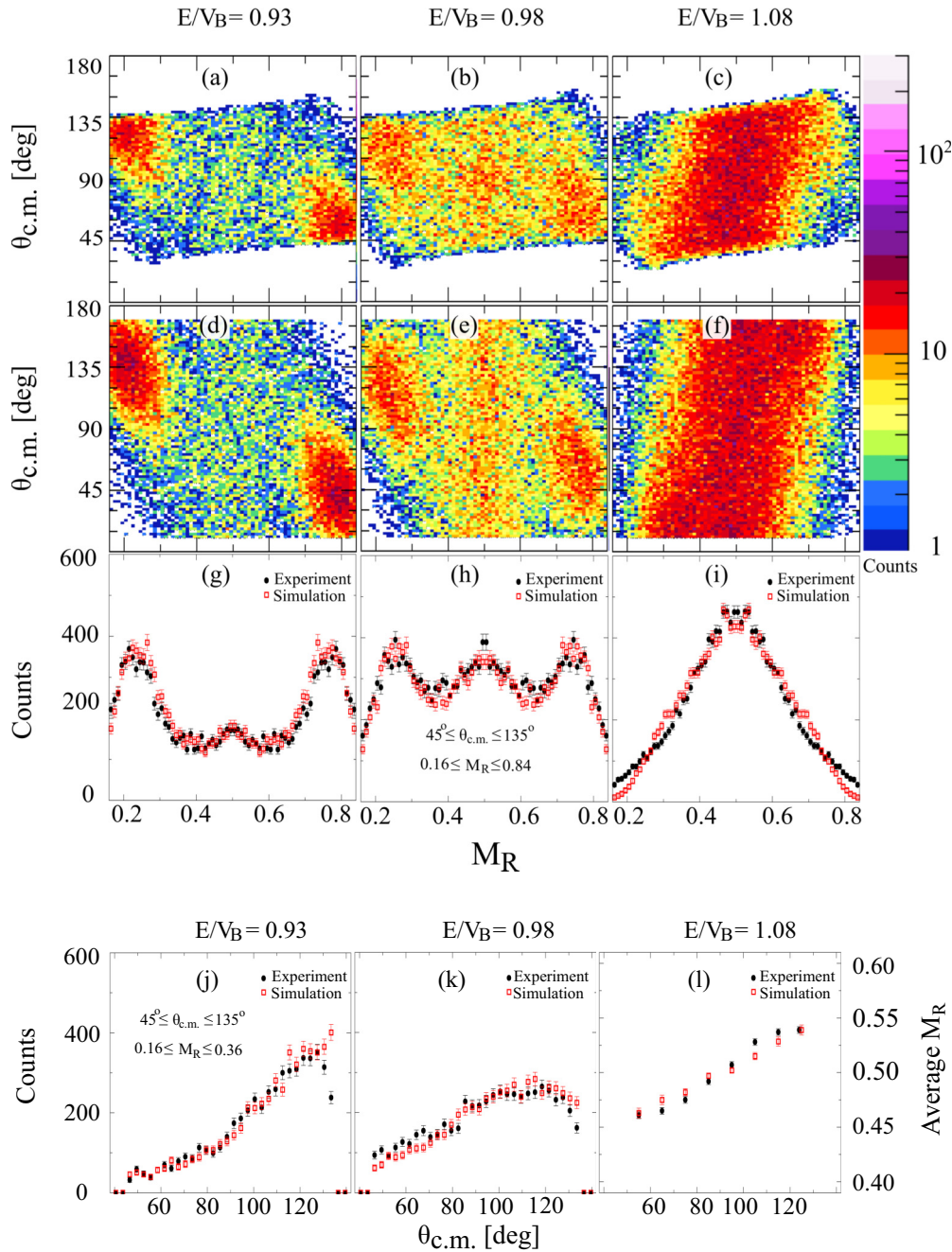


FIG. 11. Top panels (a) to (c) show experimental MAD scatter plots for the $^{34}\text{S} + ^{232}\text{Th}$ reaction at different E/V_B , showing M_R values between 0.16 and 0.84. Panels (d) to (f) show simulated MADs assuming longer mass equilibration time for fast collisions. Panels (g) to (i) show projected M_R distributions of experimental (filled black circles) and simulated (open red squares) MADs. The angular and M_R ranges used are indicated in panel (h). Bottom panels (j) and (k) show angular distributions of mass-asymmetric quasifission events from experimental (filled black circles) and simulated (open red squares) MADs at $E/V_B = 0.93$ and 0.98 for the angular and M_R windows indicated in panel (j). Bottom panel (l) shows mean M_R as a function of center-of-mass angle at $E/V_B = 1.08$.

The difference in sticking times may in part be due to the dynamics at scission, which can increase the contact time in TDHF, as the fragments move towards their asymptotic trajectories.

The failure of the standard scenario of mass evolution [3] to reproduce the experimental features of the $^{34}\text{S} + ^{232}\text{Th}$ reaction may be understood by comparing the M_R evolution

plot shown in Fig. 10(a) and the average sticking times found in this study. Töke's picture (solid black line) predicts a very rapid mass drift towards symmetry after contact. Thus mass evolves too fast towards symmetry within the 6–8 zs sticking time [the shaded region in Fig. 10(a) represents the range of average sticking times]. A smaller mass change is required to give agreement with the observed MADs in the reaction studied

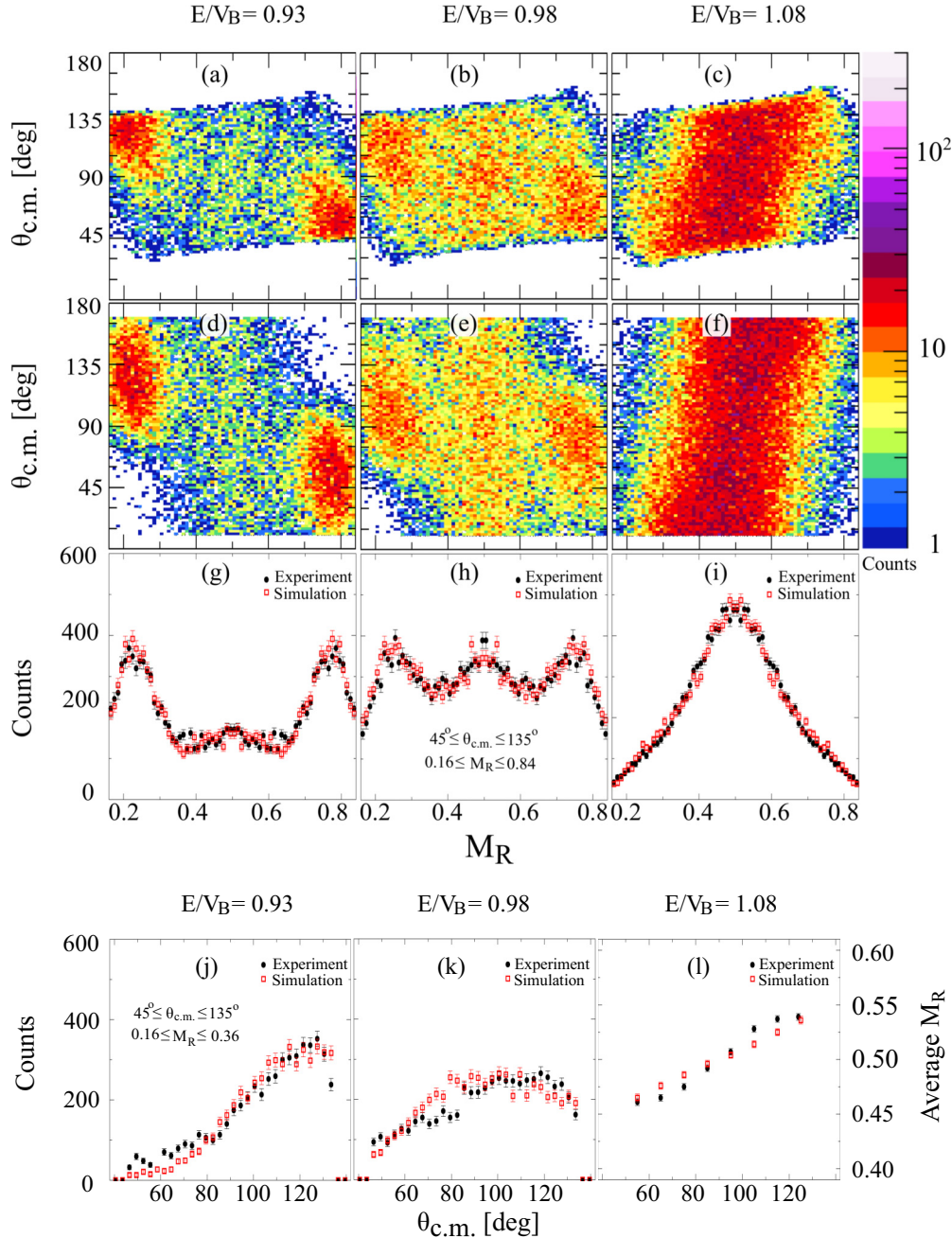


FIG. 12. Top panels (a) to (c) show experimental MAD scatter plots for the $^{34}\text{S} + ^{232}\text{Th}$ reaction at different E/V_B , showing M_R values between 0.16 and 0.84. Panels (d) to (f) show simulated MADs assuming a Fermi-type mass-drift function for slow and fast events. Panels (g) to (i) show projected M_R distributions of experimental (filled black circles) and simulated (open red squares) MADs. The angular and M_R ranges used are indicated in panel (h). Bottom panels (j) and (k) show angular distributions of mass-asymmetric quasifission events from experimental (filled black circles) and simulated (open red squares) MADs at $E/V_B = 0.93$ and 0.98 for the angular and M_R windows indicated in panel (j). Bottom panel (l) shows mean M_R as a function of center-of-mass angle at $E/V_B = 1.08$.

in this work. It is for this reason that the three alternative scenarios that match the experimental data—all show mass ratio of $M_R \approx 0.2$ at 6–8 zs, which is the average sticking time.

VIII. SUMMARY AND CONCLUSIONS

Fission-fragment mass-angle distributions have been measured for the $^{34}\text{S} + ^{232}\text{Th}$ reaction at energies around the

capture barrier. A clear transition from a dominant mass-asymmetric fast quasifission at energies below the capture barrier to predominantly mass-symmetric quasifission and fusion-fission [23] at energies above barrier is observed in the experimental MADs. The results are consistent with previous measurements [21,23,26,44] and clearly demonstrate the strong role of deformation alignment in deciding the reaction outcomes.

TABLE I. Average values of t_s distributions obtained in different pictures discussed in this work.

Picture	Average sticking time t_s (zs)		
	$E/V_B = 0.93$	$E/V_B = 0.98$	$E/V_B = 1.08$
Mass halt	8.4	6.4	7.4
τ_m varied	8.3	5.9	7.9
Fermi-type	8.1	6.3	7.0

The yield of the mass-asymmetric component is consistent with it originating from tip collisions with the deformed target nucleus and subsequent reseparation before complete mass equilibration. Importantly, the heavy asymmetric component is found to be peaked near $A = 200$ at all energies and center-of-mass angles. Similar observations were previously reported for the $^{40}\text{Ca} + ^{238}\text{U}$ reaction [28]. At the lower bombarding energies the mass-symmetric component, which largely originates from side (equatorial) collisions, is observed to be consistent with a distribution around symmetric mass division, though not necessarily resulting from fusion-fission [23].

To extract information about quasifission timescales from the data, experimental MADs were reproduced by using a Monte Carlo model assuming classical trajectories for the incoming and outgoing nuclei. Angular-momentum distributions for capture in axial and equatorial collisions using a coupled channels code, and average moments of inertia from TDHF calculations were used as inputs in these simulations. Slow (equatorial) quasifission was simulated by using a long sticking time (t_s) distribution with mass evolving asymptotically towards symmetry with $\tau_m = 5.2$ zs following Töke's [3] work. However, using this picture for the fast quasifission component failed to reproduce the experimental MADs observed in this study.

To adequately reproduce the data for the fast quasifission resulting from tip collisions, three alternative phenomenological approaches to mass evolution were tested within the Monte Carlo approach. In the first approach, a mass halt at $A = 200$ is imposed for fast quasifission. In the second approach, the mass-equilibration time constant was fit at each beam energy in order to reproduce the mass-asymmetric features of the observed MAD plots. In the third approach, a Fermi-type mass-drift function was used instead of the exponential function to model the slow mass drift during initial neck formation and last stage approaching neck rupture.

All three pictures reproduced the experimental MADs and their important features reasonably well at all energies, within the acceptance of the experimental setup. Regardless of the approach, an average sticking time between 6 and 8 zs was required for the tip (fast) events to reproduce the experimental MADs.

Although all three pictures successfully reproduced the MADs in this work, only the mass halt picture is supported by both experiment [15,28] and theoretical expectations [28]. Experimental measurements with higher statistics and wider angular coverage, together with a more sophisticated evaluation of agreement with model calculations, may be able to provide unambiguous empirical evidence for the true nature of the fast quasifission arising from the tip collisions with prolate deformed actinide nuclei.

ACKNOWLEDGMENTS

The authors acknowledge support from the Australian Research Council through Grants No. FL110100098, No. FT120100760, No. DP130101569, No. DP140101337, and No. DE140100784. Support for accelerator operations through the NCRIS program is acknowledged.

-
- [1] J. H. Hamilton, S. Hofmann, and Y. T. Oganessian, *Annu. Rev. Nucl. Part. Sci.* **63**, 383 (2013).
- [2] Y. T. Oganessian and V. K. Utyonkov, *Rep. Prog. Phys.* **78**, 036301 (2015).
- [3] J. Töke *et al.*, *Nucl. Phys. A* **440**, 327 (1985).
- [4] W. J. Świątecki, *Phys. Scr.* **24**, 113 (1981).
- [5] J. P. Blocki, H. Feldmeier and W. J. Świątecki, *Nucl. Phys. A* **459**, 145 (1986).
- [6] N. Bohr, *Nature (London)* **137**, 344 (1936).
- [7] D. J. Hinde, M. Dasgupta, and A. Mukherjee, *Phys. Rev. Lett.* **89**, 282701 (2002).
- [8] A. C. Berriman, D. J. Hinde, M. Dasgupta, C. R. Morton, R. D. Butt, and J. O. Newton, *Nature (London)* **413**, 144 (2001).
- [9] W. Q. Shen, J. Albinski, A. Gobbi, S. Gralla, K. D. Hildenbrand, N. Herrmann, J. Kuzminski, W. F. J. Müller, H. Stelzer, J. Töke, B. B. Back, S. Bjornholm, and S. P. Sorensen, *Phys. Rev. C* **36**, 115 (1987).
- [10] R. Rafiei, R. G. Thomas, D. J. Hinde, M. Dasgupta, C. R. Morton, L. R. Gasques, M. L. Brown, and M. D. Rodriguez, *Phys. Rev. C* **77**, 024606 (2008).
- [11] R. G. Thomas, D. J. Hinde, D. Duniec, F. Zenke, M. Dasgupta, M. L. Brown, M. Evers, L. R. Gasques, M. D. Rodriguez, and A. Diaz-Torres, *Phys. Rev. C* **77**, 034610 (2008).
- [12] C. J. Lin, R. du Rietz, D. J. Hinde, M. Dasgupta, R. G. Thomas, M. L. Brown, M. Evers, L. R. Gasques, and M. D. Rodriguez, *Phys. Rev. C* **85**, 014611 (2012).
- [13] E. Williams, D. J. Hinde, M. Dasgupta, R. du Rietz, I. P. Carter, M. Evers, D. H. Luong, S. D. McNeil, D. C. Rafferty, K. Ramachandran, and A. Wakhle, *Phys. Rev. C* **88**, 034611 (2013).
- [14] R. du Rietz, E. Williams, D. J. Hinde, M. Dasgupta, M. Evers, C. J. Lin, D. H. Luong, C. Simenel, and A. Wakhle, *Phys. Rev. C* **88**, 054618 (2013).
- [15] A. Wakhle, C. Simenel, D. J. Hinde, M. Dasgupta, M. Evers, D. H. Luong, R. du Rietz, and E. Williams, *Phys. Rev. Lett.* **113**, 182502 (2014).
- [16] B. B. Back, R. R. Betts, K. Cassidy, B. G. Glagola, J. E. Gindler, L. E. Glendenin, and B. D. Wilkins, *Phys. Rev. Lett.* **50**, 818 (1983).
- [17] D. J. Hinde, M. Dasgupta, J. R. Leigh, J. P. Lestone, J. C. Mein, C. R. Morton, J. O. Newton, and H. Timmers, *Phys. Rev. Lett.* **74**, 1295 (1995).

- [18] H. Q. Zhang, C. L. Zhang, C. J. Lin, Z. H. Liu, F. Yang, A. K. Nasirov, G. Mandaglio, M. Manganaro, and G. Giardina, *Phys. Rev. C* **81**, 034611 (2010).
- [19] C.-C. Sahm, H.-G. Clerc, K.-H. Schmidt, W. Reisdorf, P. Armbruster, F. P. Hessberger, J. G. Keller, G. Münzenberg, and D. Vermuelen, *Z. Phys. A: At. Nucl.* **319**, 113 (1984).
- [20] D. J. Hinde and M. Dasgupta, *Phys. Lett. B* **622**, 23 (2005).
- [21] K. Nishio *et al.*, *Phys. Rev. C* **77**, 064607 (2008).
- [22] K. Nishio *et al.*, *Phys. Rev. C* **86**, 034608 (2012).
- [23] D. J. Hinde, R. du Rietz, M. Dasgupta, R. G. Thomas, and L. R. Gasques, *Phys. Rev. Lett.* **101**, 092701 (2008).
- [24] E. M. Kozulin *et al.*, *Phys. Rev. C* **90**, 054608 (2014).
- [25] D. J. Hinde, M. Dasgupta, J. R. Leigh, J. C. Mein, C. R. Morton, J. O. Newton, and H. Timmers, *Phys. Rev. C* **53**, 1290 (1996).
- [26] D. J. Hinde, R. G. Thomas, R. du Rietz, A. Diaz-Torres, M. Dasgupta, M. L. Brown, M. Evers, L. R. Gasques, R. Rafiei, and M. D. Rodriguez, *Phys. Rev. Lett.* **100**, 202701 (2008).
- [27] G. N. Knyazheva *et al.*, *Phys. Rev. C* **75**, 064602 (2007).
- [28] C. Simenel, D. J. Hinde, R. du Rietz, M. Dasgupta, M. Evers, C. J. Lin, D. H. Luong, and A. Wakhle, *Phys. Lett. B* **710**, 607 (2012).
- [29] D. J. Hinde, M. Dasgupta, M. Evers, C. J. Lin, D. H. Luong, R. du Rietz, C. Simenel, A. Wakhle, and E. Williams, *J. Phys.: Conf. Ser.* **420**, 012115 (2013).
- [30] R. Bock *et al.*, *Nucl. Phys. A* **388**, 334 (1982).
- [31] R. du Rietz, D. J. Hinde, M. Dasgupta, R. G. Thomas, L. R. Gasques, M. Evers, N. Lobanov, and A. Wakhle, *Phys. Rev. Lett.* **106**, 052701 (2011).
- [32] W. J. Świątecki, K. Siwek-Wilczyńska, and J. Wilczyński, *Phys. Rev. C* **71**, 014602 (2005).
- [33] K. E. Rehm, A. M. van den Berg, J. J. Kolata, D. G. Kovar, W. Kutschera, G. Rosner, G. S. F. Stephans, and J. L. Yntema, *Phys. Rev. C* **37**, 2629 (1988).
- [34] W. Reisdorf, *J. Phys. G: Nucl. Part. Phys.* **20**, 1297 (1994).
- [35] B. B. Back, R. R. Betts, J. E. Gindler, B. D. Wilkins, S. Saini, M. B. Tsang, C. K. Gelbke, W. G. Lynch, M. A. McMahan, and P. A. Baisden, *Phys. Rev. C* **32**, 195 (1985).
- [36] M. Dasgupta, D. J. Hinde, N. Rowley, and A. M. Stefanini, *Annu. Rev. Nucl. Part. Sci.* **48**, 401 (1998).
- [37] A. S. Umar and V. E. Oberacker, *Nucl. Phys. A* **944**, 238 (2015).
- [38] A. S. Umar, V. E. Oberacker, and C. Simenel, *Phys. Rev. C* **92**, 024621 (2015).
- [39] M. Dasgupta, A. Navin, Y. K. Agarwal, C. V. K. Baba, H. C. Jain, M. L. Jhingan, and A. Roy, *Nucl. Phys. A* **539**, 351 (1992).
- [40] C. H. Dasso and S. Landowne, *Comput. Phys. Commun.* **46**, 187 (1987).
- [41] Ka-Hae Kim, T. Otsuka, and P. Bonche, *J. Phys. G* **23**, 1267 (1997).
- [42] M. B. Tsang, H. Utsunomiya, C. K. Gelbke, W. G. Lynch, B. B. Back, S. Saini, P. A. Baisden, and M. A. McMahan, *Phys. Lett. B* **129**, 18 (1983).
- [43] S. Szilner *et al.*, *Phys. Rev. C* **71**, 044610 (2005).
- [44] K. Nishio *et al.*, *Phys. Rev. C* **82**, 024611 (2010).